Characteristics of quantum-classical correspondence for two interacting spins

J. Emerson and L.E. Ballentine
Physics Department, Simon Fraser University, Burnaby, British Columbia, Canada V5A 1S6
(Received 7 November 2000; published 13 April 2001)

The conditions of quantum-classical correspondence for a system of two interacting spins are investigated. Differences between quantum expectation values and classical Liouville averages are examined for both regular and chaotic dynamics well beyond the short-time regime of narrow states. We find that quantum-classical differences initially grow exponentially with a characteristic exponent consistently larger than the largest Lyapunov exponent. We provide numerical evidence that the time of the break between the quantum and classical predictions scales as $\log(\mathcal{J}/\hbar)$, where $\mathcal{J}$ is a characteristic system action. However, this logarithmic break-time rule applies only while the quantum-classical deviations are smaller than $O(\hbar)$. We find that the quantum observables remain well approximated by classical Liouville averages over long times even for the chaotic motions of a few degree-of-freedom system. To obtain this correspondence it is not necessary to introduce the decoherence effects of a many degree-of-freedom environment.

DOI: 10.1103/PhysRevA.63.052103 PACS number(s): 03.65.Sq, 05.45.Mt, 03.65.Ta

I. INTRODUCTION

There is considerable interest in the interface between quantum and classical mechanics and the conditions that lead to the emergence of classical behavior. In order to characterize these conditions, it is important to differentiate two dynamical regimes of quantum-classical correspondence [1]: (i) Ehrenfest correspondence, in which the centroid of the wave packet approximately follows a classical trajectory; and (ii) Liouville correspondence, in which the quantum probability distributions are in approximate agreement with those of an appropriately constructed classical ensemble satisfying Liouville's equation.

Regime (i) is relevant only when the width of the quantum state is small compared to the dimensions of the system; if the initial state is not narrow, this regime may be absent. Regime (ii), which generally includes (i), applies to a much broader class of states, and this regime of correspondence may persist well after the Ehrenfest correspondence has broken down. The distinction between regimes (i) and (ii) has not always been made clear in the literature, though the conditions that delimit these two regimes, and in particular their scaling with system parameters, may be quite different.

The theoretical study of quantum chaos has raised the question of whether the quantum-classical break occurs differently in chaotic states, in states of regular motion, and in mixed phase-space systems. This is well understood only in the case of regime (i). There it is well known [2–4] that the time for a minimum-uncertainty wave packet to expand beyond the Ehrenfest regime scales as $\log(\mathcal{J}/\hbar)$ for chaotic states, and as a power of $\mathcal{J}/\hbar$ for regular states, where $\mathcal{J}$ denotes a characteristic system action.

The breakdown of quantum-classical correspondence, in the case of regime (ii), is less well understood, though it has been argued that this regime may also be delimited by a $\log(\mathcal{J}/\hbar)$ break time in classically chaotic states [5,6]. Some numerical evidence in support of this conjecture has been reported in a study of the kicked rotor in the *anomolous diffusion* regime [7]. (On the other hand, in the regime of *quantum localization*, the break time for the kicked rotor seems to scale as $(\mathcal{J}/\hbar)^2$ [8].) Since the $\log(\mathcal{J}/\hbar)$ time scale is rather short, it has been suggested that certain macroscopic objects would be predicted to exhibit nonclassical behavior on observable time scales [9,10]. These results highlight the importance of investigating the characteristics of quantum-classical correspondence in more detail.

In this paper we study the classical and quantum dynamics of two interacting spins. This model is convenient because the Hilbert space of the quantum system is finite dimensional, and hence tractable for computations. Spin models have been useful in the past for exploring classical and quantum chaos [3,11–15] and our model belongs to a class of spin models that shows promise of experimental realization in the near future [16]. The classical limit is approached by taking the magnitude of both spins to be very large relative to $\hbar$, while keeping their ratio fixed. For our model a characteristic system action is given by $\mathcal{J}\simeq\hbar l$, where l is a quantum number, and the classical limit is simply the limit of large quantum numbers, i.e., the limit $l\to\infty$.

In the case of the chaotic dynamics for our model, we first show that the widths of both the quantum and classical states grow exponentially at a rate given approximately by the largest Lyapunov exponent (until saturation at the system dimension). We then show that the initially small quantum-classical differences also grow at an exponential rate, with an exponent λ_{qc} that is independent of the quantum numbers and at least twice as large as the largest Lyapunov exponent. We demonstrate how this exponential growth of differences leads to a logarithmic break-time rule, $t_b\simeq\lambda_{qc}^{-1}\ln(lp/\hbar)$, delimiting the regime of Liouville correspondence. The factor p is some preset tolerance that defines a *break* between the quantum and classical expectation values. However, we also show that this logarithmic rule holds *only if* the tolerance p for quantum-classical differences is chosen extremely small, in particular $p<O(\hbar)$. For larger values of the tolerance, the break time does not occur on this logarithmic time scale and may not occur until the recurrence time. In this sense, logarithmic break-time rules describing Liouville correspondence are not robust. These results demonstrate that, for chaotic states in the classical limit, quantum observ-

ables are described approximately by Liouville ensemble averages well beyond the Ehrenfest time scale, after which both quantum and classical states relax towards equilibrium distributions. This demonstration of correspondence is obtained for a few degree-of-freedom quantum system of coupled spins that is described by a pure state and subject only to unitary evolution.

This paper is organized as follows. In Sec. II we describe the quantum and classical versions of our model. We examine the behaviors of the classical dynamics in some detail. In Sec. III we define the initial quantum states, which are SU(2) coherent states, and then define a corresponding classical density on the two-sphere which is a good analog for these states. We show in the Appendix that a perfect match is impossible: no distribution on $\mathcal{S}^2$ can reproduce the moments of the SU(2) coherent states exactly. In Sec. IV we describe our numerical techniques. In Sec. V we examine the quantum dynamics in regimes of classically chaotic and regular behavior and demonstrate the close quantitative correspondence with the Liouville dynamics that persists well after the Ehrenfest break time. In Sec. VI we characterize the growth of quantum-classical differences in the time domain. In Sec. VII we characterize the scaling of the break time for small quantum-classical differences and also examine the scaling of the maximum quantum-classical differences in the classical limit.

II. THE MODEL

We consider the quantum and classical dynamics generated by a nonintegrable model of two interacting spins,

$$H=a(S_z+L_z)+cS_xL_x\sum_{n=-\infty}^{\infty}\delta(t-n), \tag{1}$$

where $\mathbf{S}=(S_x,S_y,S_z)$ and $\mathbf{L}=(L_x,L_y,L_z)$. The first two terms in Eq. (1) correspond to a simple rotation of both spins about the z axis. The sum over the coupling terms describes an infinite sequence of δ-function interactions at times $t=n$ for integer n. Each interaction term corresponds to an impulsive rotation of each spin about the x axis by an angle proportional to the x component of the other spin.

A. The quantum dynamics

To obtain the quantum dynamics we interpret the Cartesian components of the spins as operators satisfying the usual angular-momentum commutation relations,

$$[S_i,S_j]=i\epsilon_{ijk}S_k,$$

$$[L_i,L_j]=i\epsilon_{ijk}L_k,$$

$$[J_i,J_j]=i\epsilon_{ijk}J_k.$$

In the above we have set $\hbar=1$ and introduced the total angular momentum vector $\mathbf{J}=\mathbf{S}+\mathbf{L}$.

The Hamiltonian (1) possesses kinematic constants of the motion, $[\mathbf{S}^2,H]=0$ and $[\mathbf{L}^2,H]=0$, and the total state vector $|\psi\rangle$ can be represented in a finite Hilbert space of dimension $(2s+1)\times(2l+1)$. This space is spanned by the orthonormal vectors $|s,m_s\rangle\otimes|l,m_l\rangle$, where $m_s\in\{s,s-1,\dots,-s\}$ and $m_l\in\{l,l-1,\dots,-l\}$. These are the joint eigenvectors of the four spin operators

$$\begin{aligned}\mathbf{S}^2|s,l,m_s,m_l\rangle&=s(s+1)|s,l,m_s,m_l\rangle,\\ S_z|s,l,m_s,m_l\rangle&=m_s|s,l,m_s,m_l\rangle,\\ \mathbf{L}^2|s,l,m_s,m_l\rangle&=l(l+1)|s,l,m_s,m_l\rangle,\\ L_z|s,l,m_s,m_l\rangle&=m_l|s,l,m_s,m_l\rangle.\end{aligned}\tag{2}$$

The periodic sequence of interactions introduced by the δ function produces a quantum mapping. The time evolution for a single iteration, from just before a kick to just before the next, is produced by the unitary transformation

$$|\psi(n+1)\rangle=F\,|\psi(n)\rangle, \tag{3}$$

where F is the single-step Floquet operator,

$$F=\exp[-ia(S_z+L_z)]\exp[-icS_xL_x]. \tag{4}$$

Since a is a rotation its range is 2π radians. The quantum dynamics are thus specified by two parameters, a and c, and two quantum numbers, s and l.

An explicit representation of the single-step Floquet operator can be obtained in the basis (2) by first reexpressing the interaction operator in Eq. (4) in terms of rotation operators,

$$\begin{aligned}\exp[-icS_x\otimes L_x]=&[R^{(s)}(\theta,\phi)\otimes R^{(l)}(\theta,\phi)]\exp[-icS_z\otimes L_z]\\ &\times[R^{(s)}(\theta,\phi)\otimes R^{(l)}(\theta,\phi)]^{-1},\end{aligned}\tag{5}$$

using polar angle $\theta=\pi/2$ and azimuthal angle $\phi=0$. Then the only nondiagonal terms arise in the expressions for the rotation matrices, which take the form,

$$\langle j,m'|R^{(j)}(\theta,\phi)|j,m\rangle=\exp(-im'\phi)d^{(j)}_{m',m}(\theta). \tag{6}$$

The matrix elements,

$$d^{(j)}_{m',m}(\theta)=\langle j,m'|\exp(-i\theta J_y)|j,m\rangle \tag{7}$$

are given explicitly by Wigner's formula [19].

We are interested in studying the different time-domain characteristics of quantum observables when the corresponding classical system exhibits either regular or chaotic dynamics. In order to compare quantum systems with different quantum numbers it is convenient to normalize subsystem observables by the subsystem magnitude $\sqrt{\langle\mathbf{L}^2\rangle}=\sqrt{l(l+1)}$. We denote such normalized observables with a tilde, where

$$\langle\tilde{L}_z(n)\rangle=\frac{\langle\psi(n)|L_z|\psi(n)\rangle}{\sqrt{l(l+1)}} \tag{8}$$

and the normalized variance at time n is defined as

$$\Delta\tilde{\mathbf{L}}^2(n)=\frac{\langle\mathbf{L}^2\rangle-\langle\mathbf{L}(n)\rangle^2}{l(l+1)}. \tag{9}$$

We are also interested in evaluating the properties of the quantum probability distributions. The probability distribution corresponding to the observable L_z is given by the trace

$$P_z(m_l)=\mathrm{Tr}[\rho^{(l)}(n)|l,m_l\rangle\langle l,m_l|]=\langle l,m_l|\rho^{(l)}(n)|l,m_l\rangle, \tag{10}$$

where $\rho^{(l)}(n)=\mathrm{Tr}^{(s)}[|\psi(n)\rangle\langle\psi(n)|\,|s,m_s\rangle\langle s,m_s|]$ is the reduced state operator for the spin $\mathbf{L}$ at time n and $\mathrm{Tr}^{(s)}$ denotes a trace over the factor space corresponding to the spin $\mathbf{S}$.

B. Classical map

For the Hamiltonian (1) the corresponding classical equations of motion are obtained by interpreting the angular-momentum components as dynamical variables, satisfying

$$\{S_i,S_j\}=\epsilon_{ijk}S_k,$$

$$\{L_i,L_j\}=\epsilon_{ijk}L_k,$$

$$\{J_i,J_j\}=\epsilon_{ijk}J_k,$$

with $\{\cdot,\cdot\}$ denoting the Poisson bracket. The periodic δ function in the coupling term can be used to define surfaces at $t=n$, for integer n, on which the time evolution reduces to a stroboscopic mapping,

$$\tilde{S}_x^{n+1}=\tilde{S}_x^n\cos(a)-[\tilde{S}_y^n\cos(\gamma r\tilde{L}_x^n)-\tilde{S}_z^n\sin(\gamma r\tilde{L}_x^n)]\sin(a),$$

$$\tilde{S}_y^{n+1}=[\tilde{S}_y^n\cos(\gamma r\tilde{L}_x^n)-\tilde{S}_z^n\sin(\gamma r\tilde{L}_x^n)]\cos(a)+\tilde{S}_x^n\sin(a),$$

$$\tilde{S}_z^{n+1}=\tilde{S}_z^n\cos(\gamma r\tilde{L}_x^n)+\tilde{S}_y^n\sin(\gamma r\tilde{L}_x^n), \tag{11}$$

$$\tilde{L}_x^{n+1}=\tilde{L}_x^n\cos(a)-[\tilde{L}_y^n\cos(\gamma\tilde{S}_x^n)-\tilde{L}_z^n\sin(\gamma\tilde{S}_x^n)]\sin(a),$$

$$\tilde{L}_y^{n+1}=[\tilde{L}_y^n\cos(\gamma\tilde{S}_x^n)-\tilde{L}_z^n\sin(\gamma\tilde{S}_x^n)]\cos(a)+\tilde{L}_x^n\sin(a),$$

$$\tilde{L}_z^{n+1}=\tilde{L}_z^n\cos(\gamma\tilde{S}_x^n)+\tilde{L}_y^n\sin(\gamma\tilde{S}_x^n),$$

where $\tilde{\mathbf{L}}=\mathbf{L}/|\mathbf{L}|$, $\tilde{\mathbf{S}}=\mathbf{S}/|\mathbf{S}|$ and we have introduced the parameters $\gamma=c|\mathbf{S}|$ and $r=|\mathbf{L}|/|\mathbf{S}|$. The mapping equations (11) describe the time-evolution of Eq. (1) from just before one kick to just before the next.

Since the magnitudes of both spins are conserved, $\{\mathbf{S}^2,H\}=\{\mathbf{L}^2,H\}=0$, the motion is actually confined to the four-dimensional manifold $\mathcal{P}=\mathcal{S}^2\times\mathcal{S}^2$, which corresponds to the surfaces of two spheres. This is manifest when the mapping (11) is expressed in terms of the four *canonical* coordinates $\mathbf{x}=(S_z,\phi_s,L_z,\phi_l)$, where $\phi_s=\tan(S_y/S_x)$ and $\phi_l=\tan(L_y/L_x)$. We will refer to the mapping (11) in canonical form using the shorthand notation $\mathbf{x}^{n+1}=\mathbf{F}(\mathbf{x}^n)$. It is also useful to introduce a complete set of spherical coordinates $\vec{\theta}=(\theta_s,\phi_s,\theta_l,\phi_l)$, where $\theta_s=\cos^{-1}(S_z/|\mathbf{S}|)$ and $\theta_l=\cos^{-1}(L_z/|\mathbf{L}|)$.

The classical flow (11) on the reduced surface $\mathcal{P}$ still has a rather large parameter space; the dynamics are determined from three independent dimensionless parameters: $a\in[0,2\pi)$, $\gamma\in(-\infty,\infty)$, and $r\geqslant 1$. The first of these, a, controls the angle of free-field rotation about the z axis. The parameter $\gamma=c|\mathbf{S}|$ is a dimensionless coupling strength and $r=|\mathbf{L}|/|\mathbf{S}|$ corresponds to the relative magnitude of the two spins.

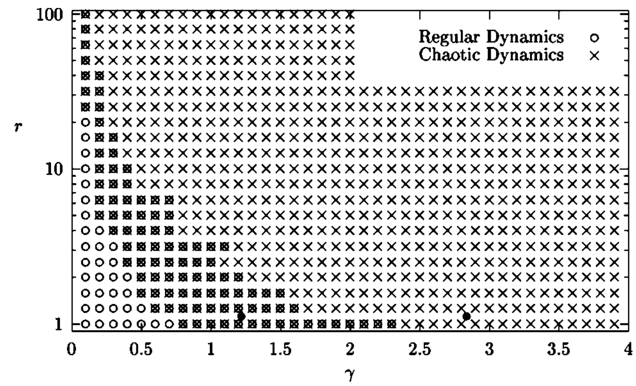

FIG. 1. Behavior of the classical mapping for different values of $r=|\mathbf{L}|/|\mathbf{S}|$ and $\gamma=c|\mathbf{S}|$ with $a=5$. Circles correspond to parameter values for which at least 99% of the surface area $\mathcal{P}$ produces regular dynamics and crosses correspond to parameter values for which the dynamics are at least 99% chaotic. Superpositions of circles and crosses correspond to parameter values that produce a mixed phase space. We investigate quantum-classical correspondence for the parameter values $\gamma=1.215$ (mixed regime) and $\gamma=2.835$ (global chaos), with $r=1.1$, which are indicated by filled circles.

We are particularly interested in the effect of increasing the coupling strength γ for different fixed values of r. In Fig. 1 we plot the dependence of the classical behavior on these two parameters for the case $a=5$, which produces typical results. The data in this figure were generated by randomly sampling initial conditions on $\mathcal{P}$, using the canonical invariant measure

$$d\mu(\mathbf{x})=d\tilde{S}_z\,d\phi_s\,d\tilde{L}_z\,d\phi_l, \tag{12}$$

and then calculating the largest Lyapunov exponent associated with each trajectory. Open circles correspond to regimes where at least 99% of the initial conditions were found to exhibit regular behavior and crosses correspond to regimes where at least 99% of these randomly sampled initial conditions were found to exhibit chaotic behavior. Circles with crosses through them (the superposition of both symbols) correspond to regimes with a mixed phase space. For the case $a=5$ and with r held constant, the scaled coupling strength γ plays the role of a perturbation parameter: the classical behavior varies from regular, to mixed, to predominantly chaotic as $|\gamma|$ is increased from zero.

The fixed points of the classical map (11) provide useful information about the parameter dependence of the classical behavior and, more importantly, in the case of mixed regimes, help locate the zones of regular behavior in the four-dimensional phase space. We find it sufficient to consider only the four trivial (parameter-independent) fixed points that lie at the poles along the z axis: two of these points correspond to parallel spins, $(S_z,L_z)=\pm(|\mathbf{S}|,|\mathbf{L}|)$, and the remaining two points correspond to antiparallel spins, $(S_z, L_z) = (\pm|\mathbf{S}|, \mp|\mathbf{L}|)$.

The stability around these fixed points can be determined from the eigenvalues of the tangent map matrix, $\mathbf{M} = \partial\mathbf{F}/\partial\mathbf{x}$, where all derivatives are evaluated at the fixed point of interest. (It is easiest to derive M using the six *non-canonical* mapping equations (11) since the tangent map for the *canonical* mapping equations exhibits a coordinate system singularity at these fixed points.) The eigenvalues corresponding to the four trivial fixed points are obtained from the characteristic equation,

$$[\xi^2 - 2\xi\cos a + 1]^2 \pm \xi^2\gamma^2 r\sin^2 a = 0, \tag{13}$$

with the minus (plus) sign corresponding to the parallel (antiparallel) cases, and we have suppressed the trivial factor $(1-\xi)^2$ that arises since the six equations (11) are not independent. For the parallel fixed points we have the four eigenvalues are

$$\xi^P_{1,2} = \cos a \pm \frac{1}{2}\sqrt{r\gamma^2\sin^2 a} + \frac{1}{2}\sqrt{\pm 4\cos a\sqrt{\gamma^2 r\sin^2 a} - (\sin^2 a)(4-\gamma^2 r)}, \tag{14}$$

$$\xi^P_{3,4} = \cos a \pm \frac{1}{2}\sqrt{r\gamma^2\sin^2 a} - \frac{1}{2}\sqrt{\pm 4\cos a\sqrt{\gamma^2 r\sin^2 a} - (\sin^2 a)(4-\gamma^2 r)},$$

and the eigenvalues for the antiparallel cases, ξ^{AP}, are obtained from Eqs. (14) through the substitution $r \to -r$. A fixed point becomes unstable if and only if $|\xi| > 1$ for at least one of the four eigenvalues.

1. Mixed phase space: γ=1.215

We are particularly interested in the behavior of this model when the two spins are comparable in magnitude. Choosing the value $r = 1.1$ (with $a = 5$ as before), we determined by numerical evaluation that the antiparallel fixed points are unstable for $|\gamma| > 0$. In the case of the parallel fixed points, all four eigenvalues remain on the unit circle, $|\xi^P| = 1$, for $|\gamma| < 1.42$. This stability condition guarantees the presence of regular islands about the parallel fixed points [20]. In Fig. 2 we plot the trajectory corresponding to the parameters $a = 5$, $r = 1.1$, $\gamma = 1.215$ and with initial condition $\vec{\theta}(0) = (5°,5°,5°,5°)$ which locates the trajectory near a stable fixed point of a mixed phase space (see Fig. 1.) This trajectory clearly exhibits a periodic pattern that we have confirmed to be regular by computing the associated Lyapunov exponent $(\lambda_L = 0)$. In contrast, the trajectory plotted in Fig. 3 is launched with the same parameters but with initial condition $\vec{\theta}(0) = (20°,40°,160°,130°)$, which is close to one of the unstable antiparallel fixed points. This trajectory explores a much larger portion of the surface of the two spheres in a seemingly random manner. As expected, a computation of the largest associated Lyapunov exponent yields a positive number $(\lambda_L = 0.04)$.

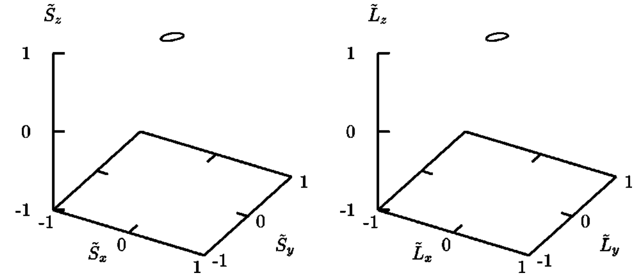

FIG. 2. Stroboscopic trajectories on the unit sphere launched from a regular zone of the mixed regime with $\gamma = 1.215$, $r = 1.1$, $a = 5$, and $\vec{\theta}(0) = (5°,5°,5°,5°)$.

2. Global chaos: γ=2.835

If we increase the coupling strength to the value $\gamma = 2.835$, with $a = 5$ and $r = 1.1$ as before, then all four trivial fixed points become unstable. By randomly sampling $\mathcal{P}$ with 3×10^4 initial conditions we find that less than 0.1% of the kinematically accessible surface $\mathcal{P}$ is covered with regular islands (see Fig. 1). This set of parameters produces a connected chaotic zone with largest Lyapunov exponent $\lambda_L = 0.45$. We will refer to this type of regime as one of ''global chaos'' although the reader should note that our usage of this expression differs slightly from that in Ref. [20].

3. The limit r≫1

Another interesting limit of our model arises when one of the spins is much larger than the other, $r \gg 1$. We expect that in this limit the larger spin (**L**) will act as a source of essentially external ''driving'' for the smaller spin (**S**). Referring to the coupling terms in the mapping (11), the driving strength, or perturbation upon **S** from **L**, is determined from the product $\gamma r = c|\mathbf{L}|$, which can be quite large, whereas the ''back-reaction'' strength, or perturbation upon **L** from **S**, is governed only by the scaled coupling strength $\gamma = c|\mathbf{S}|$, which can be quite small. It is interesting to examine whether a dynamical regime exists where the larger system might approach regular behavior while the smaller ''driven'' system is still subject to chaotic motion.

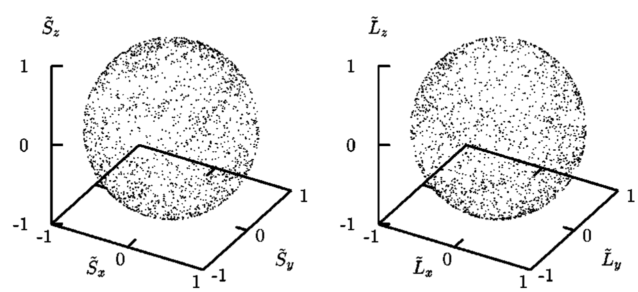

FIG. 3. Same parameters as Fig. 2, but the trajectory is launched from a chaotic zone of the mixed regime with the initial condition $\vec{\theta}(0) = (20°,40°,160°,130°)$.

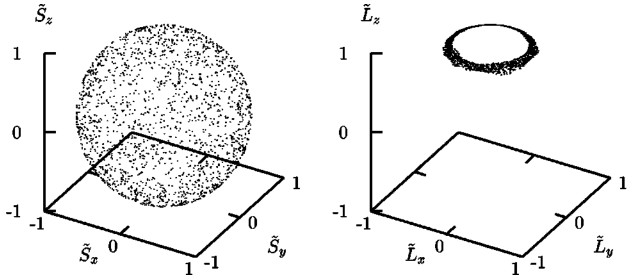

FIG. 4. A chaotic trajectory for mixed regime parameters $\gamma = 0.06$, $r=100$, and $a=5$ with $\vec{\theta}(0)=(27°,27°,27°,27°)$. The motion of the larger spin appears to remain confined to a narrow band on the surface of the sphere.

In Fig. 4 we plot a chaotic trajectory for $r=100$ with initial condition $\vec{\theta}(0)=(27°,27°,27°,27°)$, which is located in a chaotic zone ($\lambda_L=0.026$) of a mixed phase space (with $a=5$ and $\gamma=0.06$). Although the small spin wanders chaotically over a large portion of its kinematically accessible shell $\mathcal{S}^2$, the motion of the large spin remains confined to a ''narrow'' band. Although the band is narrow relative to the large spin's length, it is not small relative to the smaller spin's length. The trajectories are both plotted on the unit sphere, so the effective area explored by the large spin (relative to the effective area covered by the small spin) scales in proportion to r^2.

C. The Liouville dynamics

We are interested in comparing the quantum dynamics generated by Eq. (3) with the corresponding Liouville dynamics of a classical distribution. The time evolution of a Liouville density is generated by the partial-differential equation

$$\frac{\partial \rho_c(\mathbf{x},t)}{\partial t} = -\{\rho_c ,H\}, \tag{15}$$

where H stands for the Hamiltonian (1) and $\mathbf{x} =(S_z ,\phi_s ,L_z ,\phi_l)$.

The solution to Eq. (15) can be expressed in the compact form

$$\rho_c(\mathbf{x},t) = \int_{\mathcal{P}} d\mu(\mathbf{y})\, \delta(\mathbf{x}-\mathbf{x}(t,\mathbf{y}))\rho_c(\mathbf{y},0), \tag{16}$$

with measure $d\mu(\mathbf{y})$ given by Eq. (12) and each time-dependent function $\mathbf{x}(t,\mathbf{y})\in\mathcal{P}$ is a solution of the equations of motion for Eq. (1) with an initial condition $\mathbf{y}\in\mathcal{P}$. This integral solution (16) simply expresses that Liouville's equation (15) describes the dynamics of a classical density $\rho_c(\mathbf{x},t)$ of points evolving in phase space under the Hamiltonian flow. We exploit this fact to numerically solve Eq. (15) by randomly generating initial conditions consistent with an initial phase-space distribution $\rho_c(\mathbf{x},0)$ and then time evolving each of these initial conditions using the equations of motion (11). We then calculate the ensemble averages of dynamical variables

$$\langle \tilde{L}_z(n)\rangle_c = \int_{\mathcal{P}} d\mu(\mathbf{x}) \frac{L_z}{|\mathbf{L}|} \rho_c(\mathbf{x},n) \tag{17}$$

by summing over this distribution of trajectories at each time step.

D. Correspondence between quantum and classical models

For a quantum system specified by the four numbers $\{a,c,s,l\}$, the corresponding classical parameters $\{a,\gamma,r\}$ are determined if we associate the magnitudes of the classical angular momenta with the quantum spin magnitudes,

$$|\mathbf{S}|_c = \sqrt{s(s+1)},$$
$$|\mathbf{L}|_c = \sqrt{l(l+1)}. \tag{18}$$

This prescription produces the classical parameters,

$$r = \sqrt{\frac{l(l+1)}{s(s+1)}},$$
$$\gamma = c\sqrt{s(s+1)}, \tag{19}$$

with a the same number for both models.

We are interested in determining the behavior of the quantum dynamics in the limit $s\to\infty$ and $l\to\infty$. This is a ccomplished by studying sequences of quantum models with s and l increasing though chosen such that the classical r and γ are held fixed. Since s and l are restricted to integer (or half-integer) values, the corresponding classical r will actually vary slightly for each member of this sequence (although γ can be matched exactly by varying the quantum parameter c). In the limit $s\to\infty$ and $l\to\infty$ this variation becomes increasingly small since $r=\sqrt{l(l+1)/s(s+1)}\to l/s$. For convenience, the classical r corresponding to each member of the sequence of quantum models is identified by its value in this limit. We have examined the effect of the small variations in the value of r on the classical behavior and found the variation to be negligible.

III. INITIAL STATES

A. Initial quantum state

We consider *initial* quantum states which are pure and separable,

$$|\psi(0)\rangle = |\psi_s(0)\rangle \otimes |\psi_l(0)\rangle. \tag{20}$$

For the initial state of each subsystem we use one of the directed angular-momentum states,

$$|\theta,\phi\rangle = R^{(j)}(\theta,\phi)|j,j\rangle, \tag{21}$$

which corresponds to states of maximum polarization in the direction (θ,ϕ). It has the properties

$$\langle \theta,\phi|J_z|\theta,\phi\rangle = j\cos\theta,$$
$$\langle \theta,\phi|J_x \pm iJ_y|\theta,\phi\rangle = je^{\pm i\phi}\sin\theta, \tag{22}$$

where j in this section refers to either l or s.

The states (21) are the SU(2) coherent states, which, like their counterparts in the Euclidean phase space, are minimum uncertainty states [21]; the normalized variance of the quadratic operator,

$$\Delta\tilde{\mathbf{J}}^2=\frac{\langle\theta,\phi|\mathbf{J}^2|\theta,\phi\rangle-\langle\theta,\phi|\mathbf{J}|\theta,\phi\rangle^2}{j(j+1)}=\frac{1}{(j+1)}, \quad (23)$$

is minimized for given j and vanishes in the limit $j\rightarrow\infty$. The coherent states $|j,j\rangle$ and $|j,-j\rangle$, polarized along the z axis, also saturate the inequality of the uncertainty relation,

$$\langle J_x^2\rangle\langle J_y^2\rangle\geqslant\frac{\langle J_z\rangle^2}{4}, \quad (24)$$

although this inequality is not saturated for coherent states polarized along other axes.

B. Initial classical state and correspondence in the macroscopic limit

We compare the quantum dynamics with that of a classical Liouville density which is chosen to match the initial probability distributions of the quantum coherent state. For quantum systems with a Euclidean phase space it is always possible to construct a classical density with marginal probability distributions that match exactly the corresponding moments of the quantum coherent state. This follows from the fact that the marginal distributions for a coherent state are positive definite Gaussians, and therefore all of the moments can be matched *exactly* by choosing a Gaussian classical density. For the SU(2) coherent state, however, we show in the Appendix that no classical density has marginal distributions that can reproduce even the low-order moments of the quantum probability distributions (except in the limit of infinite j). Thus from the outset it is clear that any choice of an initial classical state will exhibit residual discrepancy in matching some of the initial quantum moments.

We have examined the initial state and dynamical quantum-classical correspondence using several different classical distributions. These included the vector model distribution described in the Appendix and the Gaussian distribution used by Fox and Elston in correspondence studies of the kicked top [22]. For a state polarized along the z axis we chose the density

$$\rho_c(\theta,\phi)\sin\theta\,d\theta\,d\phi=C\exp\left[-\frac{2\sin^2\left(\frac{\theta}{2}\right)}{\sigma^2}\right]\sin\theta\,d\theta\,d\phi$$

$$=C\exp\left[-\frac{(1-\tilde{J}_z)}{\sigma^2}\right]d\tilde{J}_z\,d\phi, \quad (25)$$

with $C=\{2\pi\sigma^2[1-\exp(-2\sigma^{-2})]\}^{-1}$, instead of those previously considered, because it is periodic under 2π rotation. An initial state directed along (θ_o,ϕ_o) is then produced by a rigid body rotation of Eq. (25) by an angle θ_o about the y axis followed by rotation with angle ϕ_o about the z axis.

The variance σ^2 and the magnitude $|\mathbf{J}|_c$ are free parameters of the classical distribution that should be chosen to fit the quantum probabilities as well as possible. It is shown in the Appendix that no classical density has marginal distributions that can match all of the quantum moments, so we concentrate only on matching the lowest-order moments. Since the magnitude of the spin is a kinematic constant, both classically and quantum mechanically, we choose the squared length of the classical spin to have the correct quantum value,

$$|\mathbf{J}|_c^2=\langle J_x^2\rangle_c+\langle J_y^2\rangle_c+\langle J_z^2\rangle_c=j(j+1). \quad (26)$$

For a state polarized along the z axis, we have $\langle J_x\rangle=\langle J_y\rangle=0$ and $\langle J_y^2\rangle=\langle J_x^2\rangle$ for both distributions as a consequence of the axial symmetry. Furthermore, as a consequence of Eq. (26), we will automatically satisfy the condition

$$2\langle J_x^2\rangle_c+\langle J_z^2\rangle_c=j(j+1). \quad (27)$$

Therefore we only need to consider the classical moments

$$\langle J_z\rangle_c=|\mathbf{J}|G(\sigma^2), \quad (28)$$

$$\langle J_x^2\rangle_c=|\mathbf{J}|^2\sigma^2G(\sigma^2), \quad (29)$$

calculated from the density (25) in terms of the remaining free parameter σ^2, where

$$G(\sigma^2)=\left[\frac{1+\exp(-2\sigma^{-2})}{1-\exp(-2\sigma^{-2})}\right]-\sigma^2. \quad (30)$$

We would like to match both of these classical moments with the corresponding quantum values,

$$\langle J_z\rangle=j, \quad (31)$$

$$\langle J_x^2\rangle=j/2, \quad (32)$$

calculated for the coherent state (21). However, no choice of σ^2 will satisfy both constraints.

If we choose σ^2 to satisfy Eq. (31) exactly then we would obtain

$$\sigma^2=\frac{1}{2j}-\frac{3}{8j^2}+O(j^{-3}). \quad (33)$$

If we choose σ^2 to satisfy (32) exactly then we would obtain

$$\sigma^2=\frac{1}{2j}+\frac{1}{4j^2}+O(j^{-3}). \quad (34)$$

[These expansions are most easily derived from the approximation $G(\sigma^2)\simeq 1-\sigma^2$, which has an exponentially small error for large j.]

We have chosen to compromise between these values by fixing σ^2 so that the ratio $\langle J_z\rangle_c/\langle J_x^2\rangle_c$ has the correct quantum value. This leads to the choice

$$\sigma^2 = \frac{1}{2\sqrt{j(j+1)}} = \frac{1}{2j} - \frac{1}{4j^2} + O(j^{-3}). \quad (35)$$

These unavoidable initial differences between the classical and quantum moments will vanish in the ''classical'' limit. To see this explicitly it is convenient to introduce a measure of the quantum-classical differences,

$$\delta J_z(n) = |\langle J_z(n)\rangle - \langle J_z(n)\rangle_c|, \quad (36)$$

defined at time n. For an initial state polarized in direction (θ,ϕ), the choice (35) produces the initial difference,

$$\delta J_z(0) = \frac{\cos(\theta)}{8j} + O(j^{-2}), \quad (37)$$

which vanishes as $j \to \infty$.

IV. NUMERICAL METHODS

We have chosen to study the time-periodic spin Hamiltonian (1) because the time dependence is then reduced to a simple mapping and the quantum state vector is confined to a finite-dimensional Hilbert space. Consequently we can solve the exact time-evolution equations (3) numerically without introducing any artificial truncation of the Hilbert space. The principal source of numerical inaccuracy arises from the numerical evaluation of the matrix elements of the rotation operator $\langle j,m'|R(\theta,\phi)|j,m\rangle = \exp(-i\phi m')d^{(j)}_{m'm}(\theta)$. The rotation operator is required both for the calculation of the initial quantum coherent state, $|\theta,\phi\rangle = R(\theta,\phi)|j,m=j\rangle$, and for the evaluation of the unitary Floquet operator. In order to maximize the precision of our results we calculated the matrix elements $d^{(j)}_{m'm}(\theta) = \langle j,m'|\exp(-i\theta J_y)|j,m\rangle$ using the recursion algorithm of Ref. [23] and then tested the accuracy of our results by introducing controlled numerical errors. For small quantum numbers ($j<50$) we are able to confirm the correctness of our coded algorithm by comparing these results with those obtained by direct evaluation of Wigner's formula for the matrix elements $d^{(j)}_{m'm}(\theta)$.

The time evolution of the Liouville density was simulated by numerically evaluating between 10^8 and 10^9 classical trajectories with randomly selected initial conditions weighted according to the initial distribution (25). Such a large number of trajectories was required in order to keep Monte Carlo errors small enough to resolve the initial normalized quantum-classical differences, which scale as $1/8j^2$, over the range of j values we have examined.

We identified initial conditions of the classical map as chaotic by numerically calculating the largest Lyapunov exponent λ_L using the formula

$$\lambda_L = \frac{1}{N}\sum_{n=1}^{N} \ln d(n), \quad (38)$$

where $d(n) = \Sigma_i|\delta x_i(n)|$, with $d(0)=1$. The differential $\delta\mathbf{x}(n)$ is a difference vector between adjacent trajectories and thus evolves under the action of the tangent map $\delta\mathbf{x}(n+1) = \mathbf{M}\cdot\delta\mathbf{x}(n)$, where $\mathbf{M}$ is evaluated along some fiducial trajectory [20].

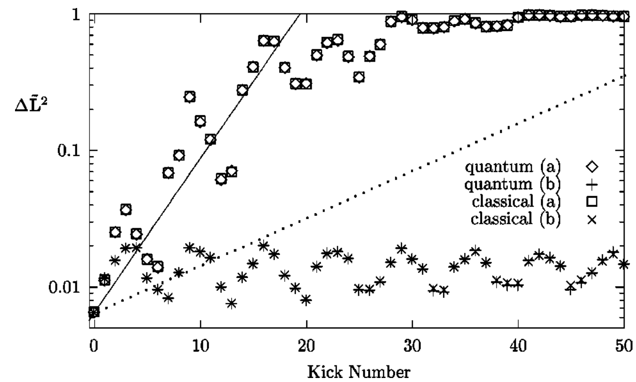

FIG. 5. Growth of normalized quantum and classical variances in a chaotic zone (a) and a regular zone (b) of the mixed phase-space regime $\gamma=1.215$ and $r\simeq1.1$ with $l=154$. Quantum and classical results are nearly indistinguishable on this scale. In the chaotic case, the approximate exponential growth of both variances is governed by a much larger rate, $\lambda_w=0.13$ (solid line), than that predicted from the largest Lyapunov exponent, $\lambda_L=0.04$ (dotted line).

Since we are interested in studying quantum states and the corresponding classical distributions that have nonzero support on the sphere, it is also important to get an idea of the size of these regular and chaotic zones. By comparing the size of a given regular or chaotic zone to the variance of an initial state located within it, we can determine whether most of the state is contained within this zone. However, we cannot perform this comparison by direct visual inspection since the relevant phase space is four dimensional. One strategy that we used to overcome this difficulty was to calculate the Lyapunov exponent for a large number of randomly sampled initial conditions and then project only those points which are regular (or chaotic) onto the plane spanned by $\tilde{S}_z = \cos\theta_s$ and $\tilde{L}_z = \cos\theta_l$. If the variance of the initial quantum state is located within, and several times smaller than, the dimensions of a zone devoid of any of these points, then the state in question can be safely identified as chaotic (or regular).

V. CHARACTERISTICS OF THE QUANTUM AND LIOUVILLE DYNAMICS

A. Mixed phase space

We consider the time development of initial quantum coherent states (21) evolved according to the mapping (3) using quantum numbers $s=140$ and $l=154$ and associated classical parameters $\gamma=1.215$, $r\simeq1.1$, and $a=5$, which produce a mixed phase space (see Fig. 1). The classical results are generated by evolving the initial ensemble (25) using the mapping (11). In Fig. 5 we compare the time dependence of the normalized quantum variance, $\Delta\tilde{\mathbf{L}}^2 = [\langle\mathbf{L}^2\rangle - \langle\mathbf{L}\rangle^2]/l(l+1)$, with its classical counterpart, $\Delta\tilde{\mathbf{L}}_c^2 = [\langle\mathbf{L}^2\rangle_c - \langle\mathbf{L}\rangle_c^2]/|\mathbf{L}|^2$. Squares (diamonds) correspond to the dynamics of an initial quantum (classical) state centered at

$\vec{\theta}(0)=(20°,40°,160°,130°)$, which is located in the connected chaotic zone near one of the unstable fixed points of the classical map. Crosses (plus signs) correspond to an initial quantum (classical) state centered on the initial condition $\vec{\theta}(0)=(5°,5°,5°,5°)$, which is located in the regular zone near one of the stable fixed points. For both initial conditions the quantum and classical results are nearly indistinguishable on the scale of the figure. In the case of the regular initial condition, the quantum variance remains narrow over long times and, like its classical counterpart, exhibits a regular oscillation. In the case of the chaotic initial condition the quantum variance also exhibits a periodic oscillation but this oscillation is superposed on a very rapid, approximately exponential, growth rate. This exponential growth persists until the variance approaches the system size, that is, when $\Delta\tilde{\mathbf{L}}^2\simeq 1$. The initial exponential growth of the quantum variance in classically chaotic regimes has been observed previously in several models and appears to be a generic feature of the quantum dynamics; this behavior of the quantum variance is mimicked very accurately by the variance of an initially well-matched classical distribution [17,22,24].

For well-localized states, in the classical case, the exponential growth of the distribution variance in chaotic zones is certainly related to the exponential divergence of the underlying trajectories, a property that characterizes classical chaos. To examine this connection we compare the observed exponential rate of growth of the widths of the classical (and quantum) state with the exponential rate predicted from the classical Lyapunov exponent. For the coherent states the initial variance can be calculated exactly, $\Delta\tilde{\mathbf{L}}^2(0)=1/(l+1)$. Then, assuming exponential growth of this initial variance, we get

$$\Delta\tilde{\mathbf{L}}^2(n)\simeq\frac{1}{l}\exp(2\lambda_w n)\quad\text{for}\quad n<t_{sat}, \tag{39}$$

where a factor of 2 is included in the exponent because $\Delta\tilde{\mathbf{L}}^2$ corresponds to a squared length. The dotted line in Fig. 5 corresponds to the prediction (39) with $\lambda_w=\lambda_L=0.04$, the value of the largest classical Lyapunov exponent. As can be seen from the figure, the actual growth rate of the classical (and quantum) variance of the chaotic initial state is significantly larger than that predicted using the largest Lyapunov exponent. For comparison purposes we also plot a solid line in Fig. 5 corresponding to Eq. (39) using $\lambda_w=0.13$, which provides a much closer approximation to the actual growth rate. We find, for a variety of initial conditions in the chaotic zone of this mixed regime, that the actual classical (and quantum) variance growth rate is consistently larger than the simple prediction (39) using λ_L for the growth rate. This systematic bias requires some explanation.

As pointed out in [22], the presence of some discrepancy between λ_w and λ_L can be expected from the fact that the Lyapunov exponent is defined as a geometric mean of the tangent map eigenvalues sampled over the entire connected chaotic zone (corresponding to the infinite time limit $n\to\infty$), whereas the *actual* growth rate of a given distribution over a small number of time steps will be determined largely by a few eigenvalues of the local tangent map. In mixed regimes these local eigenvalues will vary considerably over the phase-space manifold and the product of a few of these eigenvalues can be quite different from the geometric mean over the entire connected zone.

However, we find that the actual growth rate is consistently *larger* than the Lyapunov exponent prediction. It is well known that in mixed regimes the remnant KAM tori can be ''sticky''; these sticky regions can have a significant decreasing effect on a calculation of the Lyapunov exponent. In order to identify an initial condition as chaotic, we specifically choose initial states that are concentrated away from these KAM surfaces (regular islands). Such initial states will then be exposed mainly to the larger local expansion rates found away from these surfaces. This explanation is supported by our observations that, when we choose initial conditions closer to these remnant tori, we find that the growth rate of the variance is significantly reduced. These variance growth rates are still slightly larger than the Lyapunov rate, but this is not surprising since our initial distributions are concentrated over a significant fraction of the phase space and the growth of the distribution is probably more sensitive to contributions from those trajectories subject to large eigenvalues away from the KAM boundary than those stuck near the boundary. These explanations are further supported by the results of the following section, where we examine a phase-space regime that is nearly devoid of regular islands. In these regimes we find that the Lyapunov exponent serves as a much better approximation to the variance growth rate.

B. Regime of global chaos

If we increase the dimensionless coupling strength to $\gamma=2.835$, with $a=5$ and $r\simeq 1.1$ as before, then the classical flow is predominantly chaotic on the surface $\mathcal{P}$ (see Fig. 1). Under these conditions we expect that generic initial classical distributions (with nonzero support) will spread to cover the full surface $\mathcal{P}$ and then quickly relax close to microcanonical equilibrium. We find that the initially localized quantum states also exhibit these generic features when the quantum map is governed by parameters that produce these conditions classically.

For the nonautonomous Hamiltonian system (11) the total energy is not conserved, but the two invariants of motion, $\mathbf{L}^2$ and $\mathbf{S}^2$, confine the dynamics to the four-dimensional manifold $\mathcal{P}=\mathcal{S}^2\times\mathcal{S}^2$, which is the surface of two spheres. The corresponding microcanonical distribution is a constant on this surface, with measure (12), and zero elsewhere. From this distribution we can calculate microcanonical equilibrium values for low-order moments, where, for example, $\{L_z\}=(4\pi)^{-2}\int_{\mathcal{P}}L_z\,d\mu=0$ and $\{\Delta\mathbf{L}^2\}=\{\mathbf{L}^2\}-\{\mathbf{L}\}^2=|\mathbf{L}|^2$. The symbols $\{\cdot\}$ denote a microcanonical average.

To give a sense of the accuracy of the correspondence between the classical ensemble and the quantum dynamics in Fig. 6, we show a direct comparison of the dynamics of the quantum expectation value $\langle\tilde{L}_z\rangle$ with $l=154$ and the classical distribution average $\langle\tilde{L}_z\rangle_c$ for an initial coherent state and corresponding classical distribution centered at $\vec{\theta}=(45°,70°,135°,70°)$. To guide the eye in this figure we

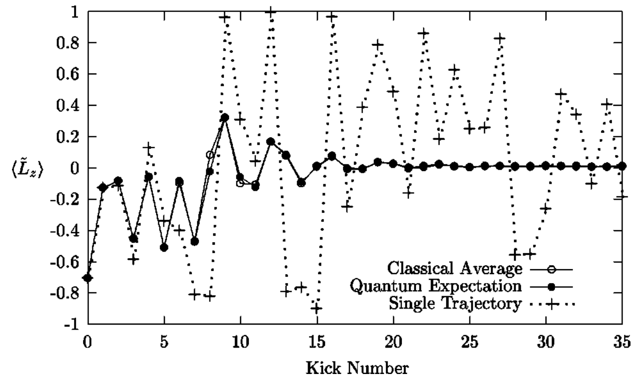

FIG. 6. Comparison of the quantum expectation value and corresponding classical average $\langle L_z \rangle_c$ in the regime of global chaos $\gamma = 2.835$ and $r \simeq 1.1$ with $l = 154$ and the initial condition $\vec{\theta}_o = (45°,70°,135°,70°)$. The points of the stroboscopic map are connected with lines to guide the eye. The quantum expectation value and the Liouville average exhibit esentially the same rate of relaxation to microcanonical equilibrium, a behavior which is qualitatively distinct from that of the single trajectory.

have drawn lines connecting the stroboscopic points of the mapping equations. The quantum expectation value exhibits essentially the same dynamics as the classical Liouville average, not only at early times, that is, in the initial Ehrenfest regime [1,25], but for times well into the equilibrium regime where the classical moment $\langle L_z \rangle$ has relaxed close to the microcanonical equilibrium value $\{L_z\} = 0$. We have also provided results for a single trajectory launched from the same initial condition in order to emphasize the qualitatively distinct behavior it exhibits.

In Fig. 7 we show the exponential growth of the normalized quantum and classical variances on a semilogarithmic plot for the same set of parameters and quantum numbers. Numerical data for (a) correspond to initial condition $\vec{\theta}(0) = (20°,40°,160°,130°)$ and those for (b) correspond to $\vec{\theta}(0) = (45°,70°,135°,70°)$. As in the mixed regime case, the quantum-classical differences are nearly imperceptible on the scale of the figure, and the differences between the quantum and classical variance growth rates are many orders of magnitude smaller than the small differences in the growth rate arising from the different initial conditions.

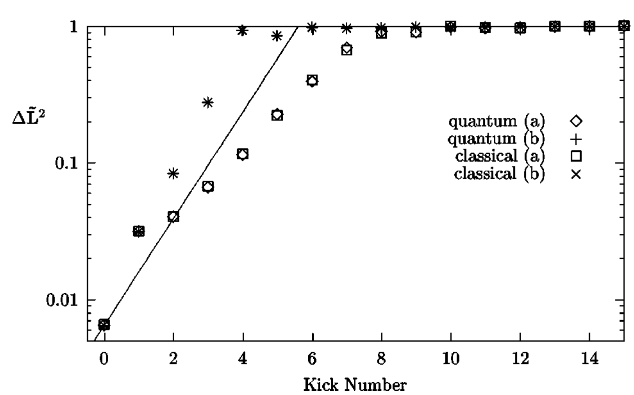

FIG. 7. Growth of normalized quantum and classical variances in the regime of global chaos, $\gamma = 2.835$ and $r \simeq 1.1$ with $l = 154$, for the two initial conditions cited in the text. Quantum-classical differences are nearly imperceptible on this scale. In this regime the largest Lyapunov exponent $\lambda_L = 0.45$ provides a much better estimate of the initial variance growth rate.

In contrast with the mixed regime case, in this regime of global chaos the prediction (39) with $\lambda_w = \lambda_L = 0.45$ now serves as a much better approximation to the exponential growth rate of the quantum variance and associated relaxation rate of the quantum and classical states. In this regime the exponent λ_w is also much larger than in the mixed regime case due to the stronger degree of classical chaos. As a result, the initially localized quantum and classical distributions saturate at system size much sooner.

It is useful to apply Eq. (39) to estimate the time scale at which the quantum (and classical) distributions saturate at system size. From the condition $\Delta \tilde{\mathbf{L}}^2(t_{sat}) \simeq 1$ and using Eq. (39) we obtain

$$t_{sat} \simeq (2\lambda_w)^{-1} \ln(l), \tag{40}$$

which serves as an estimate of this characteristic time scale. In the regimes for which the full surface $\mathcal{P}$ is predominately chaotic, we find that the actual exponential growth rate of the width of the quantum state, λ_w, is well approximated by the largest Lyapunov exponent λ_L. For $a = 5$ and $r = 1.1$, the approximation $\lambda_w \simeq \lambda_L$ holds for coupling strengths $\gamma > 2$, for which more than 99% of the surface $\mathcal{P}$ is covered by one connected chaotic zone (see Fig. 1).

By comparing the quantum probability distribution to its classical counterpart, we can learn much more about the relaxation properties of the quantum dynamics. In order to compare each m_l value of the quantum distribution $P_z(m_l)$ with a corresponding piece of the continuous classical marginal probability distribution,

$$P_c(L_z) = \int \int \int d\tilde{S}_z \, d\phi_s \, d\phi_l \, \rho_c(\theta_s, \phi_s, \theta_l, \phi_l), \tag{41}$$

we discretize the latter into $2j+1$ bins of width $\hbar = 1$. This procedure produces a discrete classical probability distribution $P_z^c(m_l)$ that prescribes the probability of finding the spin component L_z in the interval $[m_l + 1/2, m_l - 1/2]$ along the z axis.

To illustrate the time development of these distributions we compare the quantum and classical probability distributions for three successive values of the kick number n, using the same quantum numbers and initial condition as in Fig. 6. In Fig. 8 the initial quantum and classical states are both well localized and nearly indistinguishable on the scale of the figure. At time $n = 6 \simeq t_{sat}$, shown in Fig. 9, both distributions have grown to fill the accessible phase space. It is at this time that the most significant quantum-classical discrepancies appear.

For times greater than t_{sat}, however, these emergent quantum-classical discrepencies do not continue to grow, since both distributions begin relaxing towards equilibrium distributions. Since the dynamics are confined to a *compact* phase space, and in this parameter regime the remnant KAM tori fill a negligibly small fraction of the kinematicaly acces-

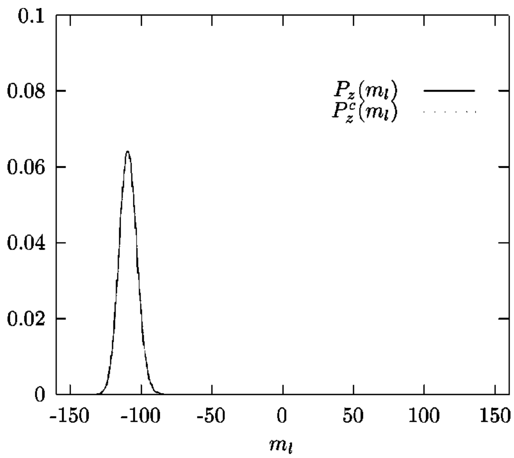

FIG. 8. Initial probability distributions for L_z for $\vec{\theta}(0) = (45°,70°,135°,70°)$ with $l = 154$. The quantum and classical distributions are indistinguishable on the scale of the figure.

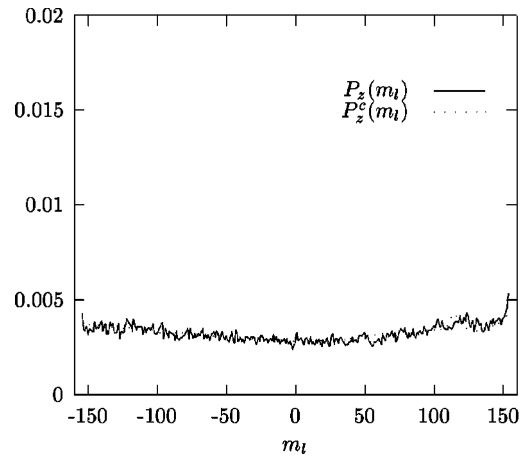

FIG. 10. Same as Fig. 9, but for $n = 15$. Both quantum and classical distributions have relaxed close to the microcanonical equilibrium.

sible phase space, we might expect the classical equilibrium distribution to be very close to the microcanonical distribution. Indeed such relaxation close to microcanonical equilibrium is apparent for both the quantum and the classical distribution at very early times, as demonstrated in Fig. 10, corresponding to $n = 15$.

Thus the signature of a classically hyperbolic flow, namely, the exponential relaxation of an arbitrary distribution (with nonzero measure) to microcanonical equilibrium [26], holds to good approximation in this model in a regime of global chaos. More suprisingly, this classical signature is manifest also in the dynamics of the quantum distribution. In the quantum case, however, as can be seen in Fig. 10, the probability distribution is subject to small irreducible time-dependent fluctuations about the classical equilibrium. We examine these quantum fluctuations in detail elsewhere [27].

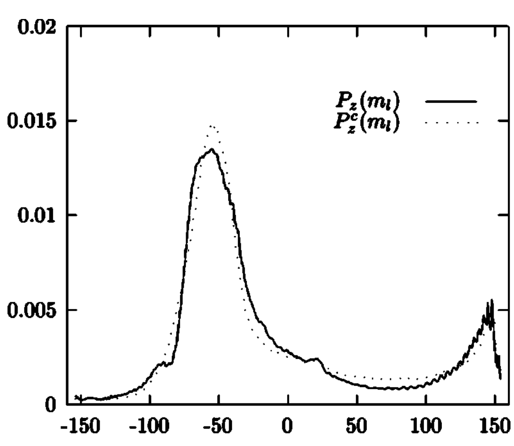

FIG. 9. Same as Fig. 8, but the states have evolved to $n = 6$ in the regime of global chaos $\gamma = 2.835$ and $r \simeq 1.1$. Both the quantum and classical distribution have spread to the system dimension and exhibit their largest differences on this saturation time scale.

VI. TIME-DOMAIN CHARACTERISTICS OF QUANTUM-CLASSICAL DIFFERENCES

We consider the time dependence of quantum-classical differences defined along the z axis of the spin **L**,

$$\delta L_z(n) = |\langle L_z(n)\rangle - \langle L_z(n)\rangle_c|, \tag{42}$$

at the stroboscopic times $t = n$. In Fig. 11 we compare the time dependence of $\delta L_z(n)$ on a semilogarithmic plot for a chaotic state (filled circles) with $\vec{\theta}(0) = (20°,40°,160°,130°)$ and a regular state (open circles), $\vec{\theta}(0) = (5°,5°,5°,5°)$, evolved using the same mixed-regime parameters ($\gamma = 1.215$ and $r \simeq 1.1$) and quantum numbers ($l = 154$) as in Fig. 5.

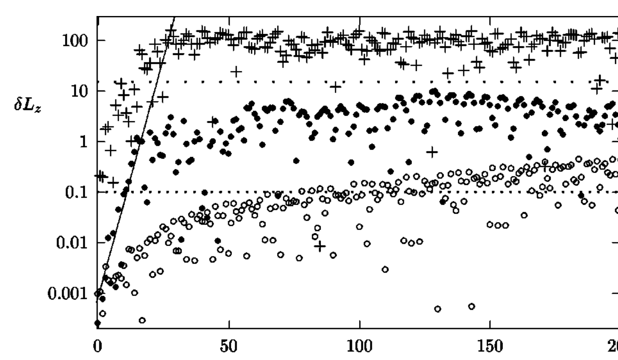

FIG. 11. Time dependence of quantum-classical differences in a regular zone (open circles) and a chaotic zone (filled circles) of mixed regime ($\gamma = 1.215$ and $r \simeq 1.1$) with $l = 154$. For the chaotic state, $\delta L_z = |\langle L_z\rangle - \langle L_z\rangle_c|$ is contrasted with the Ehrenfest difference $|\langle L_z\rangle - L_z|$ between the quantum expectation value and a single trajectory (plus signs), which grows until saturation at the system dimension. The solid line corresponds to Eq. (43) using $\lambda_{qc} = 0.43$. The horizontal lines indicate two different values of the difference tolerance p which may be used to determine the break time; for $p = 0.1$ (dotted line) t_b occurs on a logarithmic time scale, but for $p = 15.4$ (sparse dotted line) t_b is not defined over numerically accessible time scales.

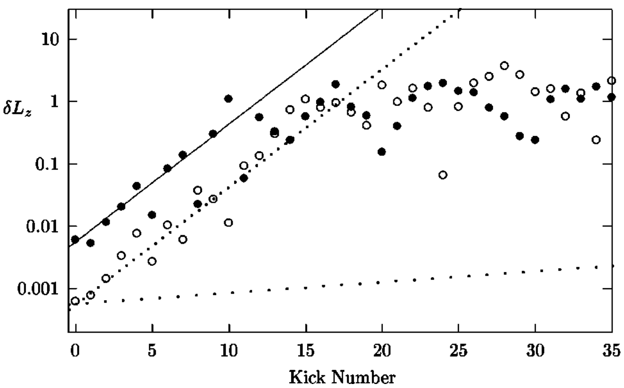

FIG. 12. Growth of the quantum-classical difference δL_z in the chaotic zone of a mixed regime, $\gamma=1.215$ and $r\simeq 1.1$, with $l=22$ (filled circles) and $l=220$ (open circles). For $l=220$ the exponential growth rate (43) is plotted using the classical Lyapunov exponent, $\lambda_L=0.04$ (sparse dotted line), and for both l values (43) is plotted using the exponent $\lambda_{qc}=0.43$ (solid line for $l=22$, dotted line for $l=220$), which is obtained from a fit of Eq. (44) to the corresponding break-time data in Fig. 14.

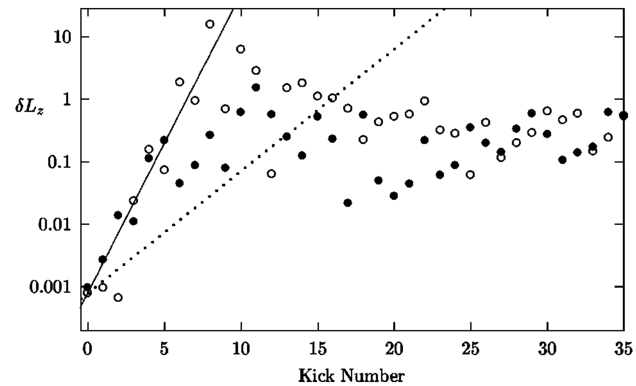

FIG. 13. Growth of quantum-classical differences in the regime of global chaos, $\gamma=2.835$ and $r\simeq 1.1$ with $l=154$, for the two initial conditions cited in text. The exponential growth rate (43) is plotted using the classical Lyapunov exponent, $\lambda_L=0.45$ (dotted line), and the exponent $\lambda_{qc}=1.1$ (solid line), which is obtained from a fit of Eq. (44) to the corresponding break-time data in Fig. 14.

We are interested in the behavior of the upper envelope of the data in Fig. 11. For the regular case, the upper envelope of the quantum-classical differences grows very slowly, as some polynomial function of time. For the chaotic case, on the other hand, at early times the difference measure (42) grows exponentially until saturation around $n=15$, which is well before reaching system dimension, $|\mathbf{L}|\simeq l=154$. After this time, which we denote t^*, the quantum-classical differences exhibit no definite growth, and fluctuate about the equilibrium value $\delta L_z \sim 1 \ll |\mathbf{L}|$. In Fig. 11 we also include data for the time dependence of the Ehrenfest difference $|\langle L_z\rangle - L_z|$, which is defined as the difference between the quantum expectation value and the dynamical variable of a single trajectory initially centered on the quantum state. In contrast to δL_z, the rapid growth of the Ehrenfest difference continues until saturation at the system dimension.

In Fig. 12 we compare the time dependence of the quantum-classical differences in the case of the chaotic initial condition $\vec{\theta}(0)=(20°,40°,160°,130°)$ for quantum numbers $l=22$ (filled circles) and $l=220$ (open circles), using the same parameters as in Fig. 11. This demonstrates the remarkable fact that the exponential growth terminates when the difference measure reaches an essentially fixed magnitude ($\delta L_z \sim 1$ as for the case $l=154$), although the system dimension differs by an order of magnitude in the two cases.

In Fig. 13 we consider the growth of the quantum-classical difference measure $\delta L_z(n)$ in a regime of global chaos, for $l=154$, and using the same set of parameters as those examined in Fig. 7 ($\gamma=2.835$ and $r\simeq 1.1$). Again the upper envelope of the difference measure $\delta L_z(n)$ exhibits exponential growth at early times, though in this regime of global chaos the exponential growth persists only for a very short duration before saturation at $t^*\simeq 6$. The initial condition $\vec{\theta}(0)=(20°,40°,160°,130°)$ is a typical case (filled circles), where, as seen for the mixed regime parameters, the magnitude of the difference at the end of the exponential growth phase saturates at the value $\delta L_z(t^*)\simeq 1$, which does not scale with the system dimension (see Fig. 15). The initial condition $\vec{\theta}(0)=(45°,70°,135°,70°)$ (open circles) leads to an anomolously large deviation at the end of the exponential growth phase, $\delta L_z(t^*)\simeq 10$, though still small relative to the system dimension $|\mathbf{L}|\simeq 154$. This deviation is transient however, and at later times the magnitude of quantum-classical differences fluctuates about the equilibrium value $\delta L_z \sim 1$. The quantum-classical differences are a factor of $1/l$ smaller than typical differences between the quantum expectation value and the single trajectory, which are of order system dimension (see Fig. 6) as in the mixed regime case.

In all cases where the initial quantum and classical states are launched from a chaotic zone we find that the initial time dependence of quantum-classical differences compares favorably with the exponential growth ansatz,

$$\delta L_z(n) \simeq \frac{1}{8l}\exp(\lambda_{qc} n) \quad \text{for} \quad n<t^*, \tag{43}$$

where the exponent λ_{qc} is a new exponent subject to numerical measurement [17]. The prefactor $1/8l$ is obtained by accounting for the initial contributions from the three Cartesian components, $[\delta^2 L_x(0)+\delta^2 L_y(0)+\delta^2 L_z(0]^{1/2}=1/8l$.

We are interested in whether the Lyapunov exponent λ_L is a good approximation to λ_{qc}. In Fig. 12 we plot Eq. (43) with $\lambda_{qc}=\lambda_L=0.04$ (dotted line) for $l=220$. Clearly the largest Lyapunov exponent severly underestimates the exponential growth rate of the quantum-classical differences, in this case by more than an order of magnitude. The growth rate of the state width, $\lambda_w=0.13$, is also several times smaller than the initial growth rate of the quantum-classical differences. In the case of Fig. 13, corresponding to a regime of global chaos with a much larger Lyapunov exponent, we plot Eq. (43) with $\lambda_{qc}=\lambda_L=0.45$ (dotted line), demonstrating that in this regime, too, the largest Lyapunov exponent underestimates the initial growth rate of the quantum-classical difference measure $\delta L_z(n)$.

We also find, from an inspection of our results, that the time t^* at which the exponential growth (43) terminates can be estimated from t_{sat}, the time scale on which the distributions saturate at or near system size (40). In the case of the chaotic initial condition of Fig. 5, for which $\gamma = 1.215$, visual inspection of the figure suggests that $t_{sat} \simeq 18$. This should be compared with Fig. 11, where the exponential growth of $\delta L_z(n)$ ends rather abruptly at $t^* \simeq 15$. In Fig. 7, corresponding to a regime of global chaos ($\gamma = 2.835$), the variance growth saturates much earlier, around $t_{sat} \simeq 6$, for both initial conditions. From Fig. 13 it is aparent that in this regime $t^* \simeq 6$. As we increase γ further, we find that the exponential growth phase of quantum-classical differences $\delta L_z(n)$ is shortened, lasting only until the corresponding quantum and classical distributions saturate at system size. For $\gamma \simeq 12$, with $\lambda_L \simeq 1.65$, the chaos is sufficiently strong that the initial coherent state for $l = 154$ spreads to cover $\mathcal{P}$ within a single time step. Similarly the initial difference measure $\delta L_z(0) \simeq 0.001$ grows to the magnitude $\delta L_z(1) \simeq 1$ within a single time step and subsequently fluctuates about that equilibrium value. We have also inspected the variation of t^* with the quantum numbers and found it to be consistent with the logarithmic dependence of t_{sat} in Eq. (40).

VII. CORRESPONDENCE SCALING IN THE CLASSICAL LIMIT

We have assumed in Eq. (43) that the exponent λ_{qc} is independent of the quantum numbers. A convenient way of confirming this, and also estimating the numerical value of λ_{qc}, is by means of a break time measure. The break time is the time $t_b(l,p)$ at which quantum-classical differences exceed some fixed tolerance p, with the classical parameters and initial condition held fixed. Setting $\delta L_z(t_b) = p$ in Eq. (43), we obtain t_b in terms of p, l, and λ_{qc},

$$t_b \simeq \lambda_{qc}^{-1} \ln(8pl) \quad \text{provided} \quad p < O(1). \tag{44}$$

The restriction $p < O(1)$, which plays a crucial role in limiting the robustness of the break-time measure (44), is explained and motivated further below.

The explicit form we have obtained for the argument of the logarithm in Eq. (44) is a direct result of our estimate that the initial quantum-classical differences arising from the Cartesian components of the spin provide the dominant contribution to the prefactor of the exponential growth ansatz (43). Differences in the mismatched higher-order moments, as well as intrinsic differences between the quantum dynamics and classical dynamics, may also contribute to this effective prefactor. We have checked that the initial value $\delta L_z(0) \simeq 1/8l$ is an adequate estimate by comparing the intercept of the quantum-classical data on a semilogarithmic plot with the prefactor of Eq. (43) for a variety of l values (see, e.g., Fig. 12).

In Fig. 14 we examine the scaling of the break time for l values ranging from 11 to 220 and with fixed tolerance $p = 0.1$. The break time can assume only the integer values $t = n$, and thus the data exhibit a step-wise behavior. For the mixed regime parameters, $\gamma = 1.215$ and $r \simeq 1.1$ (filled circles), with the initial condition $\vec{\theta}(0) = (20°, 40°, 160°, 130°)$, a nonlinear least-squares fit to Eq. (44) gives $\lambda_{qc} = 0.43$. This fit result is plotted in the figure as a solid line. The close agreement between the data and the fit provides good evidence that the quantum-classical exponent λ_{qc} is independent of the quantum numbers. To check this result against the time-dependent $\delta L_z(n)$ data, we have plotted the exponential curve (43) with $\lambda_{qc} = 0.43$ in Fig. 11 using a solid line and in Fig. 12 using a solid line for $l = 22$ and a dotted line for $l = 220$. The exponent obtained from fitting Eq. (44) serves as an excellent approximation to the initial exponential growth (43) of the quantum-classical differences in each case.

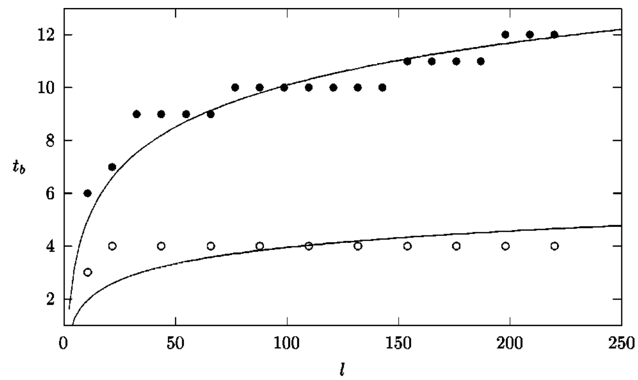

FIG. 14. Scaling of the break-time using the tolerance $p = 0.1$ as a function of increasing quantum number for the mixed regime parameters $\gamma = 1.215$ and $r \simeq 1.1$ with $\vec{\theta}(0) = (20°, 40°, 160°, 130°)$ (filled circles), and for the global chaos parameters $\gamma = 2.835$ and $r \simeq 1.1$ with $\vec{\theta}(0) = (45°, 70°, 135°, 70°)$ (open circles). We also plot the results of fits to the logarithmic rule (44), which produced exponents $\lambda_{qc} = 0.43$ for $\gamma = 1.215$ and $\lambda_{qc} = 1.1$ for $\gamma = 2.835$.

In Fig. 14 we also plot break-time results for the global chaos case $\gamma = 2.835$ and $r \simeq 1.1$ (open circles) with the initial condition $\vec{\theta}(0) = (45°, 70°, 135°, 70°)$. In this regime the quantum-classical differences grow much more rapidly and, consequently, the break time is very short and remains nearly constant over this range of computationally accessible quantum numbers. Due to this limited variation, in this regime we cannot confirm (44), although the data are consistent with the predicted logarithmic dependence on l. Moreover, the break-time results provide an effective method for estimating λ_{qc} if we assume that Eq. (44) holds. The same fit procedure as detailed above yields the quantum-classical exponent $\lambda_{qc} = 1.1$. This fit result is plotted in Fig. 14 as a solid line. More importantly, the exponential curve (43), plotted with fit result $\lambda_{qc} = 1.1$, can be seen to provide very good agreement with the initial growth rate of Fig. 13 for either initial condition, as expected.

In the mixed regime ($\gamma = 1.215$), the quantum-classical exponent $\lambda_{qc} = 0.43$ is an order of magnitude greater than the largest Lyapunov exponent $\lambda_L = 0.04$, and about three times larger than the growth rate of the width $\lambda_w = 0.13$. In the regime of global chaos ($\gamma = 2.835$) the quantum-classical exponent $\lambda_{qc}=1.1$ is a little more than twice as large as the largest Lyapunov exponent $\lambda_L=0.45$.

The condition $p<O(1)$ is a very restrictive limitation on the domain of application of the logarithmic break time (44), and it is worthwhile to explain its significance. In the mixed regime case of Fig. 11, with $l=154$, we have plotted the tolerance values $p=0.1$ (dotted line) and $p=15.4$ (sparse dotted line). The tolerance $p=0.1$ is exceeded at $t=11$, while the quantum-classical differences are still growing exponentially, leading to a logarithmic break time for this tolerance value. For the tolerance $p=15.4\ll|\mathbf{L}|$, on the other hand, the break-time does not occur on a measurable time scale, whereas according to the logarithmic rule (44), with $l=154$ and $\lambda_{qc}=0.43$, we should expect a rather short break time $t_b\simeq 23$. Consequently, the break time (44), applied to delimiting the end of the Liouville regime, is not a robust measure of quantum-classical correspondence.

Our definition of the break time (44) requires holding the tolerance p fixed in absolute terms (and not as a fraction of the system dimension as in [3]) when comparing systems with different quantum numbers. Had we chosen to compare systems using a fixed relative tolerance f, then the break time would be of the form $t_b\simeq\lambda_{qc}^{-1}\ln(8fl^2)$ and subject to the restriction $f<O(1/l)$. Since $f\rightarrow 0$ in the classical limit, this form emphasizes that the logarithmic break time applies only to differences that are a vanishing fraction of the system dimension in that limit.

Although we have provided numerical evidence (in Fig. 12) of one mixed regime case in which the largest quantum-classical differences occuring at the end of the exponential growth period remain essentially constant for varying quantum numbers, $\delta L_z(t^*)\sim O(1)$, we find that this behavior represents the typical case for all parameters and initial conditions which produce chaos classically. To demonstrate this behavior we consider the scaling (with increasing quantum numbers) of the maximum values attained by $\delta L_z(n)$ over the first 200 kicks, δL_z^{max}. Since $t^*\ll 200$ over the range of l values examined, the quantity δL_z^{max} is a rigorous upper bound for $\delta L_z(t^*)$.

In Fig. 15 we compare δL_z^{max} for the two initial conditions of Fig. 13 and using the global chaos parameters ($\gamma=2.835$, $r\simeq 1.1$). The filled circles in Fig. 15 correspond to the initial condition $\vec{\theta}(0)=(20°,40°,160°,130°)$. As in the mixed regime, the maximum deviations exhibit little or no scaling with increasing quantum number. This is the typical behavior that we have observed for a variety of different initial conditions and parameter values. These results motivate the generic rule,

$$\frac{\delta\tilde{L}_z(t^*)}{\sqrt{l(l+1)}}\leqslant\frac{\delta\tilde{L}_z^{max}}{\sqrt{l(l+1)}}\sim O(1/l). \tag{45}$$

Thus the magnitude of quantum-classical differences reached at the end of the exponential growth regime, expressed as a fraction of the system dimension, approaches zero in the classical limit.

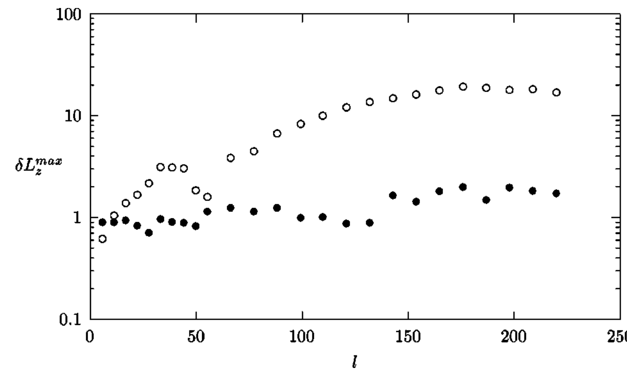

FIG. 15. Maximum quantum-classical difference occuring over the first 200 kicks in the regime of global chaos ($\gamma=2.835$, $r\simeq 1.1$) plotted against increasing quantum number. These maximum values provide an upper bound on $\delta L_z(t^*)$ for each l. The data corresponding to the initial condition $\vec{\theta}(0)=(20°,40°,160°,130°)$ (filled circles) represent a typical case in which the maximum quantum-classical differences do not vary significantly with l. The large deviations observed for the initial condition $\vec{\theta}(0)=(45°,70°,135°,70°)$ (open circles) are an exceptional case, with maximum differences growing rapidly for small quantum numbers but tending asymptotically toward independence of l. These curves provide an upper bound on the tolerance values p for which the break-time measure scales logarithmically with l.

However, for a few combinations of parameters and initial conditions we do observe a ‘‘transient’’ discrepancy peak occuring at $t\simeq t^*$ that exceeds $O(1)$. This peak is quickly smoothed away by the subsequent relaxation of the quantum and classical distributions. This peak is apparent in Fig. 13 (open circles), corresponding to the most conspicuous case that we have identified. This case is apparent as a small deviation in the normalized data of Fig. 6. The scaling of the magnitude of this peak with increasing l is plotted with open circles in Fig. 15. The magnitude of the peak initially increases rapidly, but appears to become asymptotically independent of l. The other case that we have observed occurs for the classical parameters $\gamma=2.025$, with $r\simeq 1.1$ and $a=5$, and with the initial condition $\vec{\theta}(0)=(20°,40°,160°,130°)$. We do not understand the mechanism leading to such transient peaks, although they are of considerable interest since they provide the most prominent examples of quantum-classical discrepancy that we have observed.

VIII. DISCUSSION

In this study of a nonintegrable model of two interacting spins we have characterized the correspondence between quantum expectation values and classical ensemble averages for intially localized states. We have demonstrated that in chaotic states the quantum-classical differences initially grow exponentially with an exponent λ_{qc} that is consistently larger than the largest Lyapunov exponent. In a study of the moments of the Henon-Heiles system, Ballentine and McRae [17,18] have also shown that quantum-classical differences in chaotic states grow at an exponential rate with an exponent larger than the largest Lyapunov exponent. This exponential behavior appears to be a generic feature of the short-time dynamics of quantum-classical differences in chaotic states.

Since we have studied a spin system, we have been able to solve the quantum problem without truncation of the Hilbert space, subject only to numerical roundoff, and thus we are able to observe the dynamics of the quantum-classical differences well beyond the Ehrenfest regime. We have shown that the exponential growth phase of the quantum-classical differences terminates well before these differences have reached system dimension. We find that the time scale at which this occurs can be estimated from the time scale at which the distribution widths approach the system dimension, $t_{sat} \simeq (2\lambda_w)^{-1} \ln(l)$ for initial minimum uncertainty states. Due to the close correspondence in the growth rates of the quantum and classical distributions, this time scale can be estimated from the classical physics alone. This is useful because the computational complexity of the problem does not grow with the system action in the classical case. Moreover, we find that the exponent λ_w can be approximated by the largest Lyapunov exponent when the kinematic surface is predominantly chaotic.

We have demonstrated that the exponent λ_{qc} governing the initial growth rate of quantum-classical differences is independent of the quantum numbers, and that the effective prefactor to this exponential growth decreases as $1/l$. These results imply that a logarithmic break-time rule (44) delimits the dynamical regime of Liouville correspondence. However, the exponential growth of quantum-classical differences persists only for short times and small differences, and thus this logarithmic break-time rule applies only in a similarly restricted domain. In particular, we have found that the magnitude of the differences occuring at the end of the initial exponential growth phase does not scale with the system dimension. A typical magnitude for these differences, relative to the system dimension, is $O(1/l)$. Therefore, log(l) break-time rules characterizing the end of the Liouville regime are not robust, since they apply to quantum-classical differences only in a restricted domain, i.e., to relative differences that are smaller than $O(1/l)$.

This restricted domain effect does not arise for the better known logarithmic break-time rules describing the end of the Ehrenfest regime [1–3]. The Ehrenfest logarithmic break time remains robust for arbitrarily large tolerances, since the corresponding differences grow roughly exponentially until saturation at the system dimension [22,24]. Consequently, a log(l) break time indeed implies a *breakdown* of Ehrenfest correspondence. However, the logarithmic break-time rule characterizing the end of the Liouville regime does not imply a breakdown of Liouville correspondence because it does not apply to the observation of quantum-classical discrepancies larger than $O(1/l)$. The appearance of residual $O(1/l)$ quantum-classical discrepancies in the description of a macroscopic body is, of course, consistent with quantum mechanics having a proper classical limit.

We have found, however, that for certain exceptional combinations of parameters and initial conditions there are relative quantum-classical differences occuring at the end of the exponential growth phase that can be larger than $O(1/l)$, though still much smaller than the system dimension. In absolute terms, these transient peaks seem to grow with the system dimension for small quantum numbers, but become asymptotically independent of the system dimension for larger quantum numbers. Therefore, even in these least favorable cases, the *fractional* differences between quantum and classical dynamics approach zero in the limit $l \rightarrow \infty$. This vanishing of fractional differences is sufficient to ensure a classical limit for our model.

Finally, contrary to the results found in the present model, it has been suggested that a logarithmic break time delimiting the Liouville regime implies that certain isolated macroscopic bodies in chaotic motion should exhibit nonclassical behavior on observable time scales. However, since such nonclassical behavior is not observed in the chaotic motion of macroscopic bodies, it is argued that the observed classical behavior emerges from quantum mechanics only when the quantum description is expanded to include interactions with the many degrees of freedom of the ubiquitous environment [9,10]. (This effect, called decoherence, rapidly evolves a pure system state into a mixture that is essentially devoid of nonclassical properties.) However, in our model the classical behavior emerges in the macroscopic limit of a few degree-of-freedom quantum system that is described by a pure state and subject only to unitary evolution. Quantum-classical correspondence at both early and late times arises in spite of the logarithmic break time because this break-time rule applies only when the quantum-classical difference threshold is chosen smaller than $O(\hbar)$. In this sense we find that the decoherence effects of the environment are not necessary for correspondence in the macroscopic limit. Of course the effect of decoherence may be experimentally significant in the quantum and mesoscopic domains, but it is not required *as a matter of principle* to ensure a classical limit.

ACKNOWLEDGMENTS

We wish to thank F. Haake and J. Weber for drawing our attention to the recursion algorithm for the rotation matrix elements published in [23]. J.E. would like to thank K. Kallio for stimulating discussions. We acknowledge financial support from the Natural Sciences and Engineering Research Council of Canada.

APPENDIX

Ideally, we would like to construct an initial classical density that reproduces all of the moments of the initial quantum coherent states. This is possible in a Euclidean phase space, in which case all Weyl-ordered moments of the coherent state can be matched exactly by the moments of a Gaussian classical distribution. However, we prove that no classical density $\rho_c(\theta,\phi)$ that describes an ensemble of spins of fixed length $|\mathbf{J}|$ can be constructed with marginal distributions that match those of the SU(2) coherent states (21). Specifically, we consider the set of distributions on $\mathcal{S}^2$ with continuous independent variables $\theta \in [0,\pi]$ and $\phi \in [0,2\pi)$, measure $d\mu = \sin\theta\, d\theta\, d\phi$, and subject to the usual normalization,

$$\int_{\mathcal{S}^2} d\mu\, \rho_c(\theta,\phi) = 1. \tag{A1}$$

For convenience we choose the coherent state to be polarized along the positive-z axis, $\rho = |j,j\rangle\langle j,j|$. This state is axially symmetric: rotations about the z axis by an arbitrary angle ϕ leave the state operator invariant. Consequently, we require axial symmetry of the corresponding classical distribution,

$$\rho_c(\theta,\phi) = \rho_c(\theta). \tag{A2}$$

We use the expectation of the quadratic operator, $\langle \mathbf{J}^2\rangle = j(j+1)$, to fix the length of the classical spins,

$$|\mathbf{J}| = \sqrt{\langle J^2\rangle_c} = \sqrt{j(j+1)}. \tag{A3}$$

Furthermore, the coherent state $|j,j\rangle$ is an eigenstate of J_z with moments along the z axis given by $\langle J_z^n\rangle = j^n$ for integer n. Therefore we require that the classical distribution produces the moments

$$\langle J_z^n\rangle_c = j^n. \tag{A4}$$

These requirements are satisfied by the δ-function distribution

$$\rho_v(\theta) = \frac{\delta(\theta-\theta_o)}{2\pi \sin\theta_o}, \tag{A5}$$

where $\cos\theta_o = j/|\mathbf{J}|$ defines θ_o. This distribution is the familiar vector model of the old quantum theory corresponding to the intersection of a cone with the surface of the sphere.

However, in order to derive an inconsistency between the quantum and classical moments we do not need to assume that the classical distribution is given explicitly by Eq. (A5); we only need to make use of the the azimuthal invariance condition (A2), the length condition (A3), and the first two even moments of Eq. (A4).

First we calculate some of the quantum coherent state moments along the x axis (or any axis orthogonal to z),

$$\langle J_x^m\rangle = 0 \quad \text{for odd } m,$$

$$\langle J_x^2\rangle = j/2,$$

$$\langle J_x^4\rangle = 3j^2/4 - j/4.$$

In the classical case, these moments are of the form

$$\langle J_x^m\rangle_c = \int dJ_z \int d\phi\, \rho_c(\theta) |\mathbf{J}|^m \cos^m(\phi) \sin^m(\theta). \tag{A6}$$

For m odd the integral over ϕ vanishes, as required for correspondence with the odd quantum moments. For m even we can evaluate Eq. (A6) by expressing the right-hand side as a linear combination of the z-axis moments (A4) of equal and lower order. For $m=2$ this requires substituting $\sin^2(\theta) = 1 - \cos^2(\theta)$ into Eq. (A6) and then integrating over ϕ to obtain

$$\langle J_x^2\rangle_c = \pi \int dJ_z\, \rho_c(\theta) |\mathbf{J}|^2 - \pi \int dJ_z\, \rho_c(\theta) |\mathbf{J}|^2 \cos^2(\theta)$$
$$= |\mathbf{J}|/2 - \langle J_z^2\rangle/2.$$

Since $\langle J_z^2\rangle$ is determined by Eq. (A4) and the length is fixed from Eq. (A3) we can deduce the classical value without knowing $\rho(\theta)$,

$$\langle J_x^2\rangle_c = j/2. \tag{A7}$$

This agrees with the value of the corresponding quantum moment. For $m=4$, however, by a similar procedure we deduce

$$\langle J_x^4\rangle_c = 3j^2/8, \tag{A8}$$

which differs from the quantum moment $\langle J_x^4\rangle$ by the factor

$$\delta J_x^4 = |\langle J_x^4\rangle - \langle J_x^4\rangle_c| = |3j^2/8 - j/4|, \tag{A9}$$

concluding our proof that no classical distribution on $\mathcal{S}^2$ can reproduce the quantum moments.

[1] L.E. Ballentine, Y. Yang, and J.P. Zibin, Phys. Rev. A **50**, 2854 (1994).
[2] G.P. Berman and G.M. Zaslavsky, Physica A **91A**, 450 (1978).
[3] F. Haake, M. Kus, and R. Scharf, Z. Phys. B: Condens. Matter **65**, 361 (1987).
[4] B.V. Chirikov, F.M. Israilev, and D.L. Shepelyansky, Physica D **33**, 77 (1988).
[5] W.H. Zurek and J.P. Paz, Phys. Rev. Lett. **72**, 2508 (1994).
[6] S. Habib, K. Shizume, and W.H. Zurek, Phys. Rev. Lett. **80**, 4361 (1998).
[7] R. Roncaglia, L. Bonci, B.J. West, and P. Grigolini, Phys. Rev. E **51**, 5524 (1995).
[8] F. Haake, *Quantum Signatures of Chaos* (Springer-Verlag, New York, 1991).
[9] W.H. Zurek and J.P. Paz, Phys. Rev. Lett. **75**, 351 (1995).
[10] W.H. Zurek, Phys. Scr. **T76**, 186 (1998).
[11] M. Feingold and A. Peres, Physica D **9**, 433 (1983).
[12] L.E. Ballentine, Phys. Rev. A **44**, 4126 (1991).
[13] L.E. Ballentine, Phys. Rev. A **44**, 4133 (1991).
[14] L.E. Ballentine, Phys. Rev. A **47**, 2592 (1993).
[15] D.T. Robb and L.E. Reichl, Phys. Rev. E **57**, 2458 (1998).
[16] G.J. Milburn, e-print quant-ph/9908037.
[17] L.E. Ballentine and S.M. McRae, Phys. Rev. A **58**, 1799 (1998).
[18] L.E. Ballentine, Phys. Rev. A **63**, 024101 (2001).
[19] J.J. Sakurai, *Modern Quantum Mechanics* (Benjamin-Cummings, Menlo Park, CA, 1985).
[20] A.J. Lichtenberg and M.A. Lieberman, *Regular and Chaotic*

Motion (Springer-Verlag, New York, 1992).
[21] A. Perelomov, *Generalized Coherent States and Their Applications* (Springer-Verlag, New York, 1986).
[22] R.F. Fox and T.C. Elston, Phys. Rev. E **50**, 2553 (1994).
[23] A. Braun, P. Gerwinski, F. Haake, and H. Schomerus, Z. Phys. B: Condens. Matter **100**, 115 (1996).
[24] R.F. Fox and T.C. Elston, Phys. Rev. E **49**, 3683 (1994).
[25] B.S. Helmkamp and D.A. Browne, Phys. Rev. E **49**, 1831 (1994).
[26] J.R. Dorfman, *An Introduction to Chaos in NonEquilibrium Statistical Mechanics* (Cambridge University Press, Cambridge, England, 1999).
[27] J. Emerson and L.E. Ballentine, e-print quant-ph/0103050.